Why does the tippedisk invert? Theory and experiments

Simon Sailer and Remco I. Leine
Institute for Nonlinear Mechanics, University of Stuttgart, Stuttgart, Germany

Summary. The *Tippedisk* is a mechanical-mathematical archetype for a peculiar friction-induced inversion phenomenon that occurs when the disk is spun rapidly about an in-plane axis, with the center of gravity rising counterintuitively as the orientation of the disk inverts. To qualitatively understand the dynamical behavior of the tippedisk, a nonlinear analysis is performed leading to a singularly perturbed structure of the system equations. Application of singular perturbation theory implies the study of the long-term behavior on a two-dimensional slow manifold, which finally allows to qualitatively explain the non-intuitive inversion behavior. Due to the technical simplicity of the system, the pronounced nonlinear behavior can be easily compared with real experiments.

Introduction

In the scientific research community, there are various gyroscopic systems which are interacting with a frictional support, such as Euler's disk [1], the rattleback [2], the tippetop [3], and the nonlinear dynamics of rolling basketballs [4]. Because of their technical simplicity, these systems lead to low-dimensional system equations that are ideally suited for the application of nonlinear dynamics theory. The tippetop [5, 6], as well as the related dynamics of spinning eggs [7], correspond to a subclass of gyroscopic systems, which show a counterintuitive rise of the center of gravity (COG), caused by friction-induced instability phenomena. This behavior is counterintuitive since the potential energy increases with the height of the center of gravity, which can be observed directly by eye. The decrease in kinetic energy, on the other hand, can not be detected without measurement because the change in spinning speed is relatively small. The tippedisk, being basically a rigid eccentric disk, was introduced in [9] as a new mechanical-mathematical archetype for a peculiar friction-induced inversion phenomenon that exhibits inversion behavior when rotated rapidly about an in-plane axis, see Fig. 1. The mechanical model derived in [9] forms the basis for the following analysis and was reduced in [10], accompanied by a local stability analysis. We aim to conduct an in-depth stability analysis for the tippedisk

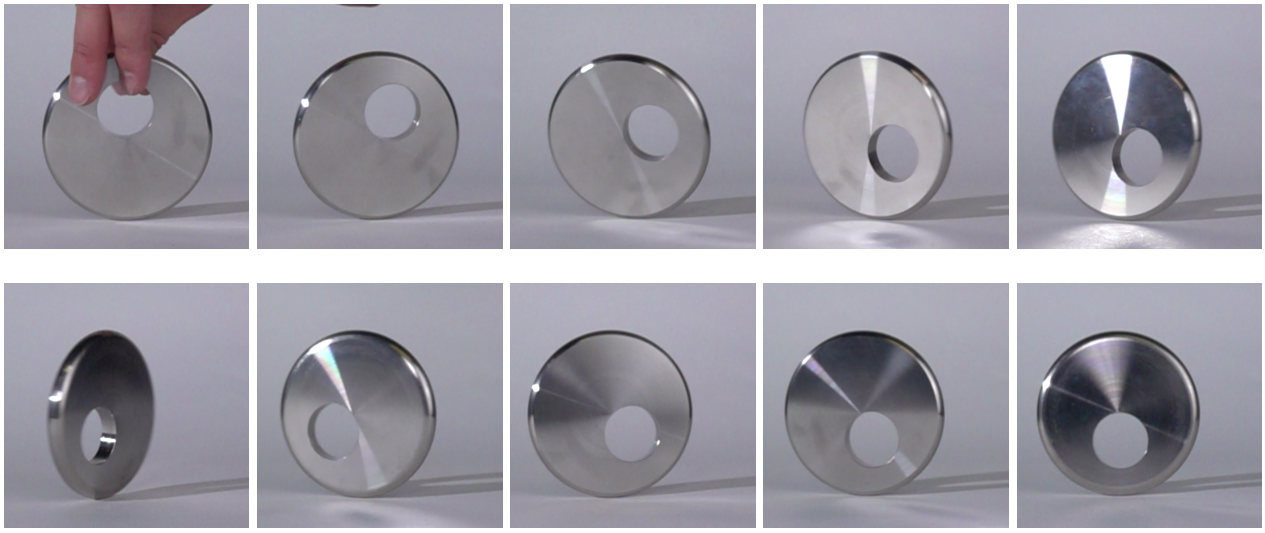

Figure 1: Tippedisk: stroboscopic sequence of the inversion phenomenon.

in order to qualitatively understand the global behavior. In an experimental setup, the qualitative dynamics of the mathematical model can be compared with the dynamic behavior of the real system.

Mechanical model

In [10] a minimal mechanical model was derived, which is able to describe the inversion phenomenon of the tippedisk. The mechanical system consists of an infinitely thin unbalanced disk, with mass m, radius r and eccentricity e. The simplest way to design such a disk, where the COG and the geometric center G do not coincide, is to take a homogeneous disk and to drill a hole (remove mass) at an arbitrary point, which does not coincide with the geometric center G of the disk. As the tippedisk does not detach during inversion, the unilateral constraint at the contact point C can be equivalently replaced by a bilateral one. In Figure 2, the mechanical model is shown.

The body-fixed B-frame is attached to the disk, such that $\mathbf{e}_z^B$ lies perpendicular to the surface of the disk. The $\mathbf{e}_x^B$-vector is defined as the normalized vector of $\mathbf{r}_{GS}$, which points from the geometric center G to the center of gravity S. To describe the contact point C, we introduce the grinding G-frame, in which $\mathbf{r}_{GC} = -r\,\mathbf{e}_y^G$ holds. The comparison with a quaternion based model implies that Euler angles α, β and γ, in common z-x-z-convention, are sufficient to describe the inversion phenomenon of the disk, see [9]. The angle α corresponds to the spinning angle, which describes the rotation around a vertical $\mathbf{e}_z^I$-axis. The inclination of the disk is measured by the inclination angle β, while γ describes the rolling angle of the disk.

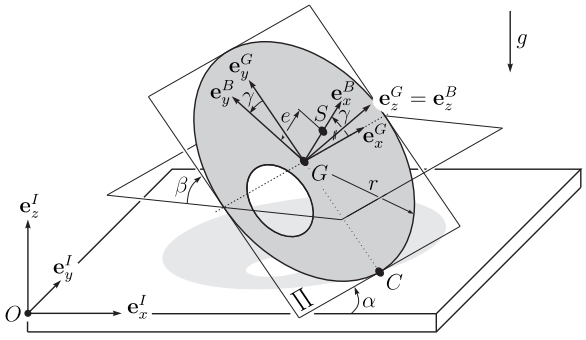

Figure 2: Mechanical model: tippedisk

Dimensions

The dimensions of the considered specimen can be found in Fig. 3 and Table 1. In the previous works [9, 10, 11], the inertial properties were approximated by an assumed density and simplified geometry. In order to ensure better comparability between simulation and experiment, a more exact calculation of the mass and inertia properties is performed here. Therefore, the mass $m = 0.425\,\mathrm{kg}$ of the considered specimen was measured directly on a calibrated scale.

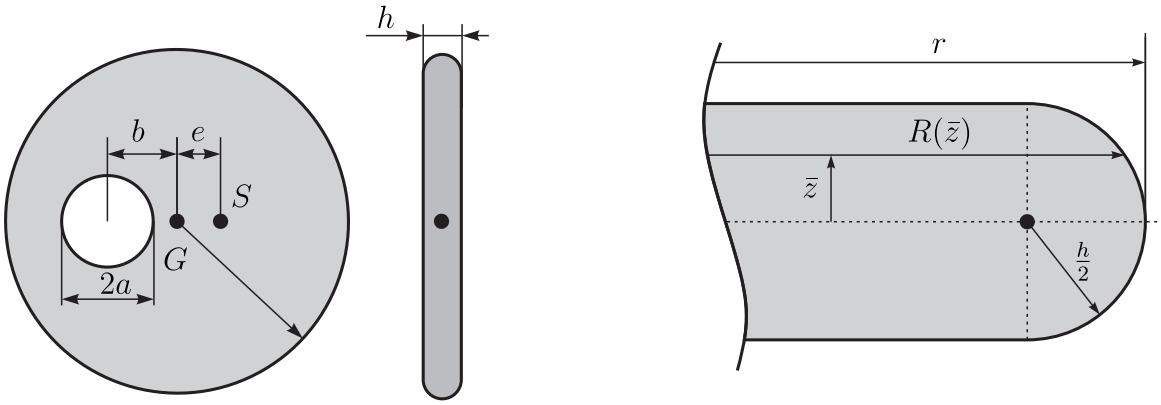

Figure 3: Geometry of the tippedisk

Table 1: Dimensions of the tippedisk

Property	Parameter	Magnitude	Unit
Disk radius	r	0.045	m
Hole radius	a	0.015	m
Distance	b	0.02	m
Disk height	h	0.01	m
Volume	V	$5.359 \cdot 10^{-5}$	m^3

Table 2: Mass properties of the tippedisk

Property	Parameter	Magnitude	Unit
Mass	m	0.425	kg
Density	ρ	7930	$\mathrm{kg/m}^3$
Eccentricity	e	$2.64 \cdot 10^{-3}$	m
${}_B\boldsymbol{\Theta}_G(1,1)$	A	$0.233 \cdot 10^{-3}$	$\mathrm{kg\ m}^2$
${}_B\boldsymbol{\Theta}_G(2,2)$	B	$0.211 \cdot 10^{-3}$	$\mathrm{kg\ m}^2$
${}_B\boldsymbol{\Theta}_G(3,3)$	C	$0.437 \cdot 10^{-3}$	$\mathrm{kg\ m}^2$

In Fig. 3 it is shown that the radius

$$R(\bar{z}) = r - \frac{h}{2} + \sqrt{\left(\frac{h}{2}\right)^2 - \bar{z}^2} \tag{1}$$

of the rounding depends on the $\bar{z}$ coordinate. Under consideration of this rounded edge, the volume yields a triple integral

$$V = \pi h(r^2 - a^2) - \int_0^{2\pi} \int_{-\frac{h}{2}}^{+\frac{h}{2}} \int_{R(\bar{z})}^{r} \bar{r}\,\mathrm{d}\bar{r}\mathrm{d}z\mathrm{d}\varphi \tag{2}$$

and, after a little algebra, the corresponding solution for the total volume V of the disk is given as

$$V = \pi h(r^2 - a^2) + \pi \left(\frac{h}{2}\right)^2 \left[\left(\frac{5}{3} - \frac{\pi}{2}\right) h + (\pi - 4)r\right] = 5.359 \cdot 10^{-5}\,\mathrm{m}^3. \tag{3}$$

Assuming a homogeneous material, the specific mass density is equal to the relation $\rho = \frac{m}{V}$ of weighed mass m and calculated total volume V, yielding $\rho = 7930 \frac{\mathrm{kg}}{\mathrm{m}^3}$. With this density ρ and the dimensions of the unbalanced disk, the inertia properties are calculated with sufficient accuracy using the commercial CAD software 'SolidWorks' and are listed in Table 2.

Singularly perturbed equations of motion

In [10] a reduction of the full model equations was derived to reduce the dimension of the state-space. It turned out that the horizontal position of the COG can be neglected during the inversion process. The spinning speed $\Omega = \dot{\alpha}$ changes only slightly and therefore can be set approximately constant, which allows to introduce the spinning speed Ω as bifurcation parameter.
Defining the new minimal coordinates $\mathbf{z} = [\beta,\ \gamma]^{\mathrm{T}}$ and the scalar[1] minimal velocity $\mathbf{v} = \dot{\beta}$, the dynamic behavior under longitudinal rolling of the disk is completely described by the system of equations

$$\begin{aligned} \dot{\mathbf{z}} &= \mathbf{B}(\mathbf{z})\mathbf{v} + \boldsymbol{\beta}(\mathbf{z}) \\ \mathbf{M}(\mathbf{z})\dot{\mathbf{v}} - \mathbf{h}(\mathbf{z},\mathbf{v}) &= -\frac{\mu m g}{\varepsilon}\mathbf{w}_y\gamma_y, \end{aligned} \tag{4}$$

with $\mathbf{B}(\mathbf{z}) = [1,\ 0]^{\mathrm{T}}$ and $\boldsymbol{\beta}(\mathbf{z}) = [0,\ -\Omega\cos\beta]^{\mathrm{T}}$ defining the kinematics. The mass matrix $\mathbf{M}$ and the vector of gyroscopic and gravitational forces $\mathbf{h}$ are given as

$$\mathbf{M} = A\cos^2\gamma + \bar{B}\sin^2\gamma + m(r + e\sin\gamma)^2\cos^2\beta, \tag{5}$$

and

$$\begin{aligned} \mathbf{h} = &+(A\cos^2\gamma + \bar{B}\sin^2\gamma)\Omega^2\sin\beta\cos\beta \\ &- 2(A - \bar{B})\Omega\dot{\beta}\cos\beta\sin\gamma\cos\gamma \\ &+ m(r + e\sin\gamma)^2\dot{\beta}^2\sin\beta\cos\beta \\ &+ me(r + e\sin\gamma)\Omega^2\sin\beta\cos^3\beta\sin\gamma \\ &- me(r + e\sin\gamma)(3\sin^2\beta - 2)\Omega\dot{\beta}\cos\beta\cos\gamma \\ &- mg(r + e\sin\gamma)\cos\beta, \end{aligned} \tag{6}$$

where the auxiliary variable $\bar{B} := B - me^2$ has been used. The right-hand side contains the generalized force direction

$$\mathbf{w}_y = (r + e\sin\gamma)\sin\beta, \tag{7}$$

and the lateral sliding velocity

$$\gamma_y = (r + e\sin\gamma)\dot{\beta}\sin\beta - e\Omega\sin^2\beta\cos\gamma. \tag{8}$$

The friction and smoothing coefficients are assumed to be $\mu = 0.3$ and $\varepsilon = 0.1\frac{\mathrm{m}}{\mathrm{s}}$. A more detailed derivation of the reduced equations of motion can be found in [10].

According to [11], the dynamics of the tippedisk must be considered on two different timescales, as Eq. 4 yields a singularly perturbed structure. Introducing the slow variables $\mathbf{x} = [\beta,\ \gamma]^{\mathrm{T}}$ and the fast variable $\mathbf{y} = \eta = \dot{\beta}$, we obtain the singularly perturbed dynamical system

$$\begin{aligned} \dot{\mathbf{x}} &= \mathbf{f}(\mathbf{x},\mathbf{y}) \\ \varepsilon\,\dot{\mathbf{y}} &= \mathbf{g}(\mathbf{x},\mathbf{y};\varepsilon) = \mathbf{g}_0(\mathbf{x},\mathbf{y}) + \mathbf{g}_1(\mathbf{x},\mathbf{y})\,\varepsilon, \end{aligned} \tag{9}$$

with

$$\mathbf{f}(\mathbf{x},\mathbf{y}) = \begin{bmatrix} \eta \\ -\Omega\cos\beta \end{bmatrix} \in \mathbb{R}^2, \tag{10}$$

$$\mathbf{g}_0(\mathbf{x},\mathbf{y}) = -\mathbf{M}^{-1}\mu m g\,\mathbf{w}_y(\mathbf{x})\gamma_y(\mathbf{x},\mathbf{y}) \in \mathbb{R}, \tag{11}$$

and

$$\mathbf{g}_1(\mathbf{x},\mathbf{y}) = \mathbf{M}^{-1}\mathbf{h}(\mathbf{x},\mathbf{y}) \in \mathbb{R}, \tag{12}$$

by normalizing and pre-multiplying Eq. (4) with the 'small' smoothing coefficient $\varepsilon > 0$ of the friction law, cf. [12]. The fast subsystem is then given as

$$\varepsilon\,\dot{\mathbf{y}} = \mathbf{g}(\mathbf{x},\mathbf{y};\varepsilon) = \mathbf{g}_0(\mathbf{x},\mathbf{y}) + \mathbf{g}_1(\mathbf{x},\mathbf{y})\,\varepsilon. \tag{13}$$

[1] Although the minimal velocity is scalar, we stick to vector notation and write $\mathbf{v}$ to keep the singularly perturbed equations of motion in a general, mechanical structure.

For $\varepsilon = 0$, the fast dynamics degenerates to the algebraic equation $\mathbf{g}_0(\mathbf{x}, \mathbf{y}) = 0$, which, according to Eq (11), states that the relative velocity $\gamma_y(\mathbf{x}, \mathbf{y})$ vanishes, i.e., the contact point of the tippedisk is in a state of pure rolling. Since the relative lateral sliding velocity $\gamma_y(\mathbf{x}, \mathbf{y})$ depends linearly on the fast variable $\eta = \dot{\beta}$, the critical manifold exists globally since the Jacobian $\frac{\partial \mathbf{g}_0}{\partial \mathbf{y}}\big|_{\mathbf{x},\mathbf{y}}$ is invertible. The corresponding critical manifold $\mathcal{M}_c$ is given as

$$\mathcal{M}_c := \left\{ (\mathbf{x}, \mathbf{y}) \in \mathbb{R}^3 |\ \mathbf{y} = \mathbf{h}_c(\mathbf{x}) = \frac{e \sin\beta \cos\gamma}{(r + e\sin\gamma)} \Omega \ , \mathbf{x} \in \mathbb{R}^2 \right\}, \tag{14}$$

being the zero order approximation of the slow manifold, which is given up to orders $\mathcal{O}(\varepsilon^2)$ as

$$\mathcal{M}_s := \left\{ (\mathbf{x}, \mathbf{y}) \in \mathbb{R}^3 |\ \mathbf{y} = \frac{e \sin\beta \cos\gamma}{(r + e\sin\gamma)} \Omega + \mathbf{h}_1(\mathbf{x})\varepsilon + \mathcal{O}(\varepsilon^2) \ , \mathbf{x} \in \mathbb{R}^2 \right\}, \tag{15}$$

with

$$\mathbf{h}_1(\mathbf{x}) = \frac{\partial \mathbf{g}}{\partial \mathbf{y}}\bigg|^{-1}_{\mathbf{x},\mathbf{h}_c} \left[\frac{\partial \mathbf{h}_c}{\partial \mathbf{x}}\bigg|_{\mathbf{x}} \mathbf{f}(\mathbf{x}, \mathbf{h}_c) - \mathbf{g}_1(\mathbf{x}, \mathbf{h}_c) \right]. \tag{16}$$

The stability of the slow manifold, characterized by the distance dynamics

$$\mathbf{d}' = \frac{\partial \mathbf{g}_0}{\partial \mathbf{y}}\bigg|_{\mathbf{x},\mathbf{h}_c} \mathbf{d}, \tag{17}$$

is asymptotically stable, since the Jacobian

$$\frac{\partial \mathbf{g}_0}{\partial \mathbf{y}}\bigg|_{\mathbf{x},\mathbf{h}_c} = -\mathbf{M}^{-1} \mu m g \, (r + e\sin\gamma)^2 \sin^2\beta \tag{18}$$

is strictly negative for all $\beta \in (0, +\pi)$, i.e., in a basin of attraction the orbits are attracted by the invariant manifold $\mathcal{M}_s$. Therefore, the asymptotic behavior of attracted solutions is governed by the reduced two-dimensional system

$$\begin{aligned} &\mathbf{h}_s(\mathbf{x}) \approx \mathbf{h}_c(\mathbf{x}) + \varepsilon \mathbf{h}_1(\mathbf{x}) \\ &\dot{\mathbf{x}} = \mathbf{f}\left(\mathbf{x}, \mathbf{h}_s(\mathbf{x})\right), \end{aligned} \tag{19}$$

neglecting orders $\mathcal{O}(\varepsilon^2)$.

Qualitative dynamics of the tippedisk

According to the simplification of the systems equations, performed in [10], and the singularly perturbed structure, discussed in [11], the qualitative dynamics of the tippedisk can be analyzed in the β-γ-space. Within this representation, we must first characterize the stationary spinning states of the disk, namely 'non-inverted' and 'inverted' spinning. Figure. 4 shows the two possible stationary spinning solutions of the tippedisk.

With respect to the chosen parametrization of the disk, the non-inverted stationary spinning corresponds to the point ($\beta = +\frac{\pi}{2}, \gamma = -\frac{\pi}{2}$). Inverted spinning is characterized by ($\beta = +\frac{\pi}{2}, \gamma = +\frac{\pi}{2}$). Due to trigonometric ambiguity, both stationary spinning solutions occur with 2π periodicity in the rolling angle γ, i.e., the point ($\beta = \frac{\pi}{2}, \gamma = +\frac{3\pi}{2}$) can be also identified as non-inverted spinning equilibrium. During the inversion, the disk remains almost in a vertical plane, so the inclination can be restricted to the interval $\beta \in [\frac{\pi}{3}, \frac{3\pi}{4}]$.

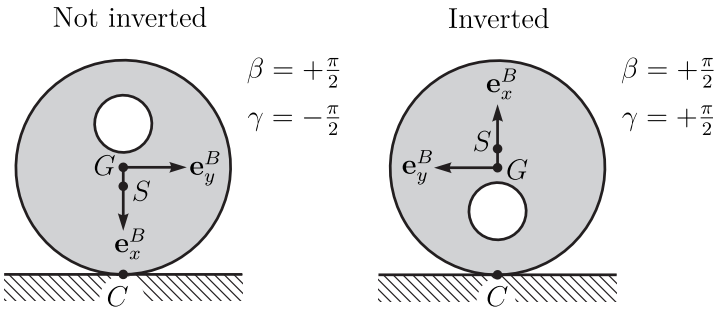

Figure 4: Stationary spinning solutions of the tippedisk

According to the linear stability analysis of [10], the equilibrium corresponding to 'non-inverted spinning' is unstable for any spinning speed Ω. The stability of 'inverted spinning' solutions is characterized by a supercritical Hopf-bifurcation at the critical spinning speed Ω_{crit}, being approximately given in closed-form as

$$\Omega_{\text{crit}} = \sqrt{\frac{(r+e)^2}{r} \frac{mg}{B - me^2}} = 30.21 \, \frac{\text{rad}}{\text{s}}. \tag{20}$$

At slow spinning speeds $\Omega < \Omega_{\text{crit}}$, the inverted spinning of the disk is unstable, and stable at supercritical spinning velocities $\Omega > \Omega_{\text{crit}}$. Following [11], the dynamical behavior on the slow manifold $\mathcal{M}_s$ is shown in

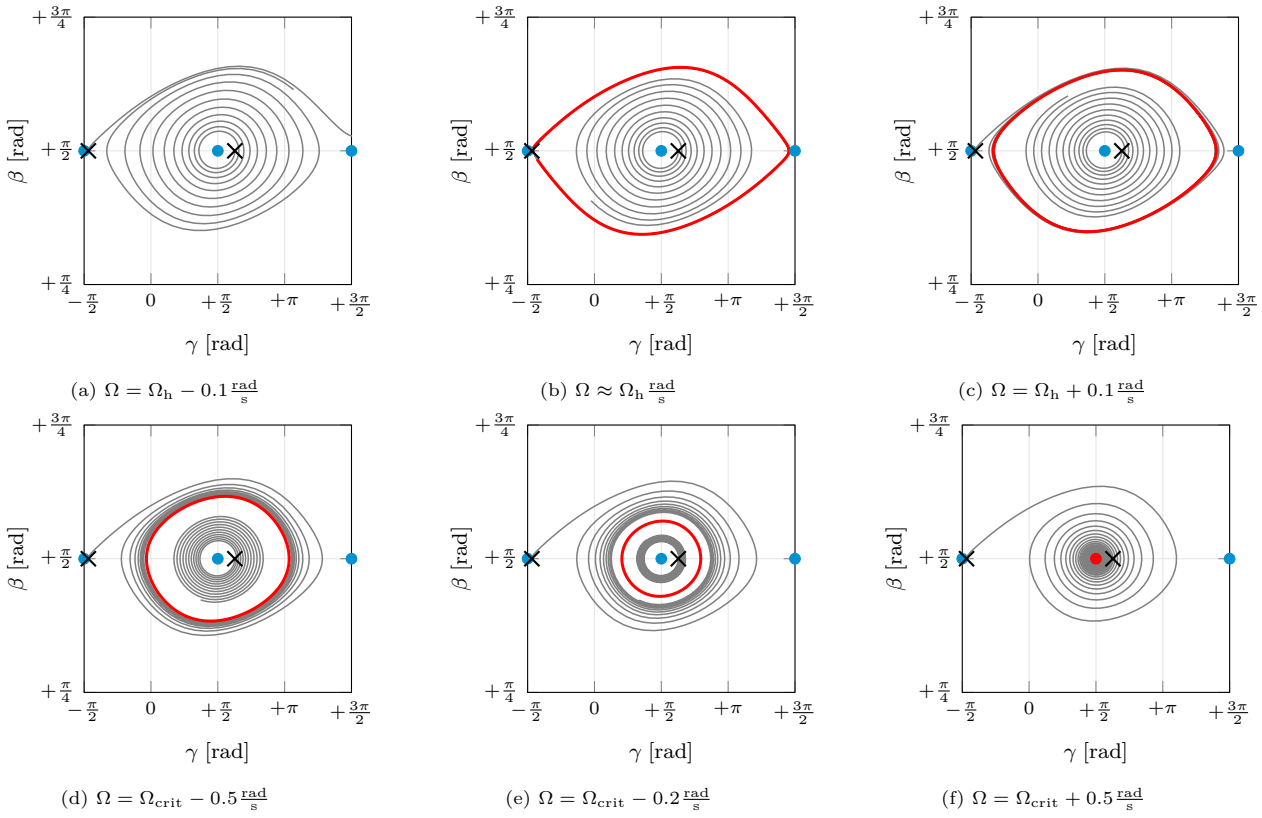

(a) $\Omega = \Omega_\mathrm{h} - 0.1\,\frac{\mathrm{rad}}{\mathrm{s}}$ (b) $\Omega \approx \Omega_\mathrm{h}\,\frac{\mathrm{rad}}{\mathrm{s}}$ (c) $\Omega = \Omega_\mathrm{h} + 0.1\,\frac{\mathrm{rad}}{\mathrm{s}}$

(d) $\Omega = \Omega_\mathrm{crit} - 0.5\,\frac{\mathrm{rad}}{\mathrm{s}}$ (e) $\Omega = \Omega_\mathrm{crit} - 0.2\,\frac{\mathrm{rad}}{\mathrm{s}}$ (f) $\Omega = \Omega_\mathrm{crit} + 0.5\,\frac{\mathrm{rad}}{\mathrm{s}}$

Figure 5: Qualitative dynamics in (β, γ)-plane: Solutions which are depicted in gray are initialized at the corresponding black cross and are obtained by time integration over the time span $\Delta t = 10\,\mathrm{s}$. Stable periodic solutions (red) originate from numerical shooting.

Fig. 5, using the corrected mass and inertia properties from Table-2. To study the dynamical behavior, we assume that the angular velocity $\dot{\alpha} = \Omega$ is constant, which identifies the bifurcation parameter Ω and leads to a foliation of the state-space. The evolution of solutions for different spinning speeds Ω are shown in β-γ-space, Fig. 5. Two unstable 'non-inverted spinning' configurations correspond to the points $(\beta = \frac{\pi}{2}, \gamma = -\frac{\pi}{2})$ and $(\beta = \frac{\pi}{2}, \gamma = \frac{3\pi}{2})$ and are shown in light blue. The inverted configuration is characterized by the dot at $(\beta = \frac{\pi}{2}, \gamma = \frac{\pi}{2})$. Unstable inverted spinning is indicated by a blue dot, stable inverted spinning by a red dot. At time $t_0 = 0\,\mathrm{s}$, two solutions are initialized at the black crosses at $\mathbf{x}_0^1 = (\beta = \frac{\pi}{2}, \gamma = -\frac{\pi}{2} + 0.1)$ and $\mathbf{x}_0^2 = (\beta = \frac{\pi}{2}, \gamma = \frac{\pi}{2} + 0.4)$ for each subfigure. The resulting trajectories are shown as gray curves. For $\Omega < \Omega_\mathrm{h}$, solutions are repelled by the inverted spinning equilibrium (Fig. 5a). At $\Omega_\mathrm{h} \approx 29.3\,\frac{\mathrm{rad}}{\mathrm{s}}$, a periodic solution (with period time $T = \infty$) arises connecting two non-inverted stationary spinning solutions (Fig. 5b). This connection can be interpreted as two heteroclinic connections because two different equilibrium points $(\beta = \frac{\pi}{2}, \gamma = -\frac{\pi}{2})$ and $(\beta = \frac{\pi}{2}, \gamma = \frac{3\pi}{2})$ are connected. From a physical point of view, this connection can also be called a homoclinic, since both connected points describe inverted spinning. If the spinning speed is increased but still subcritical, i.e., $\Omega_\mathrm{h} < \Omega < \Omega_\mathrm{crit}$ holds, solutions are attracted by a stable periodic orbit that shrinks with increasing spinning velocity Ω (Figs. 5c-5e). Due to the supercritical Hopf-bifurcation, the periodic solution vanishes at Ω_crit. For supercritical spinning speeds, i.e., $\Omega > \Omega_\mathrm{crit}$, the inverted spinning equilibrium is stable (shown as red dot), so that the solutions converge asymptotically to the inverted spinning configuration (Fig. 5f), which qualitatively explains the inversion phenomenon.

Experiments

In order to verify the validity of the qualitative dynamics of the tippedisk, presented in [11], preliminary experiments were performed. This was done with the help of an object tracking system that combines the measurements of six high-speed cameras, each of which records the movement of the disk from a different angle and at 500 frames per second. Figure 6a, shows a post-processed image of one high-speed camera with different marker frames. In Figs. 6b and 6c, the spinning angle α and the projection of the state onto the β-γ-plane are shown for four different runs, each starting with a different initial spinning velocity Ω_i^* and all initialized near non-inverted spinning motion. With time, the spinning speed Ω, which is the time derivative of the spinning angle α, gradually decreases due to dissipation caused by frictional forces. The black and the dark gray trajectories belong to very fast spinning speeds and quickly settle near the inverted spinning motion. The gray trajectory is at an intermediate initial spinning speed Ω_3^* and is reminiscent of the periodic limit cycle

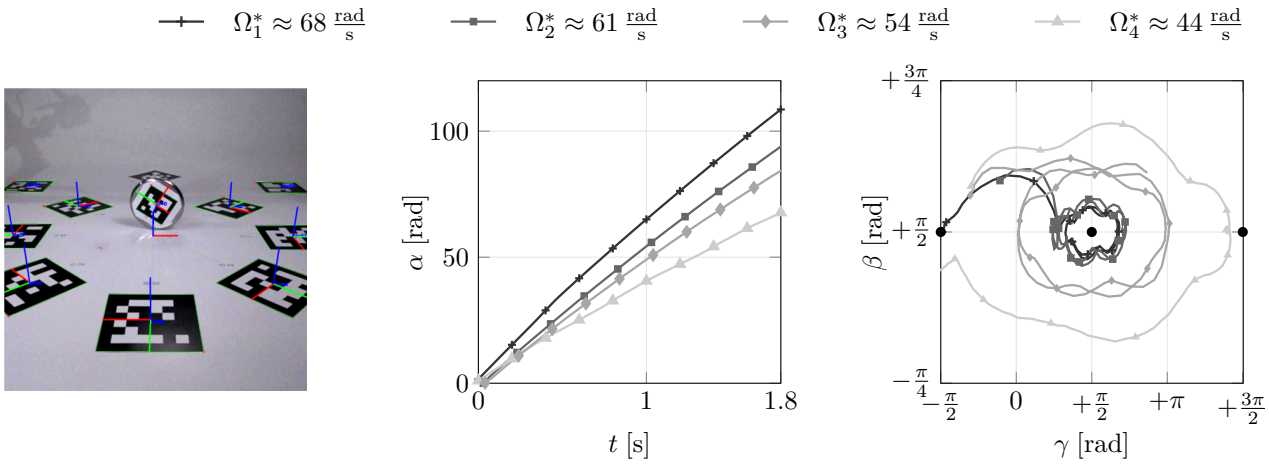

(a) Example of one processed high-speed video.

(b) Experimental obtained evolution of the spinning angle α

(c) Experimental obtained dynamics projected into the β-γ-space

Figure 6: Experiments of the tippedisk. All solutions are starting in the neighborhood of non-inverted stationary spinning at different initial spinning speeds.

between heteroclinic and Hopf bifurcation. Finally, the light gray trajectory appears to be qualitatively close to the heteroclinic connection. The measurements seem to agree with the qualitative behavior of the reduced model derived in [11]. Comparing the spinning speeds, the initial rotational velocity Ω_i^* does not match the magnitude of the bifurcation parameter Ω of the reduced model, with similar qualitative inversion behavior. This discrepancy seems to be due to the decrease in angular velocity and needs to be analyzed in future research.

Conclusions

In this work, the dynamic analysis of the tippedisk was studied based on a minimal mechanical model that contains the relevant effects and is able to describe the inversion phenomenon of the tippedisk. Consideration of the singularly perturbed structure allows the dynamics to be reduced to a two-dimensional system, so that the origin of the inversion phenomenon can be studied in the corresponding reduced system. An in-depth analysis suggests a bifurcation scenario in which a heteroclinic bifurcation accompanied by the emergence of an attractive periodic solution is followed by a supercritical Hopf bifurcation in which this periodic solution disappears. Closed-form expressions approximately characterize the associated critical spinning velocity Ω_{crit}. When the corresponding bifurcation point is crossed, the inverted configuration becomes stable and subsequently attracts almost all solutions. Preliminary experiments shown in Fig. 6 support the results of the qualitative analysis from [11] of the reduced model derived in [10]. By studying the mechanical system at all model levels and in conjunction with experimental observations, the nonlinear behavior of the tippedisk can finally be understood and the magic behind the phenomenon of inversion revealed.
Therefore, the tippedisk forms a wonderful archetype system for friction-induced instabilities, linking analytical and nonlinear dynamics with applied mechanics and allowing the comparison of the qualitative behavior of a mechanical model with experiments on a real specimen.

References

[1] Leine R.I. (2009) Experimental and theoretical investigation of the energy dissipation of a rolling disk during its final stage of motion. *Arch Appl Mech* **79**:1063-1082.

[2] Borisov A.V., Mamaev I.S. (2003) Strange attractors in rattleback dynamics. Physics-Uspekhi **46**:393–403.

[3] Bou-Rabee N.M., Marsden J.E., Romero L.A. (2004) Tippe Top inversion as a dissipation-induced instability. *SIAM J. Appl. Dyn. Syst.* **3**, 352-377.

[4] Antali M., Havas V., Hogan S.J., Stepan G. (2021) Nonlinear dynamics of a basketball rolling around the rim. *Nonlinear Dyn.* **104**, 3013-3037.

[5] Magnus K. (1971) Kreisel. Springer, Berlin; Heidelberg; New York.

[6] Cohen R.J. (1977) The tippe top revisited; *American Journal of Physics* **45**:12-17.

[7] Moffatt K., Shimomura Y. (2002) Classical dynamics: Spinning eggs — a paradox resolved. *Nature* **416**:385–386.

[8] Leine R.I., Glocker Ch. (2003) A set-valued force law for spatial Coulomb–Contensou friction. *Eur. J. Mech. A/Solids*, **22**:193-216.

[9] Sailer S., Eugster S.R., Leine R.I. (2020) The Tippedisk: a Tippetop Without Rotational Symmetry. *Regul. Chaot. Dyn.* **6**:553–580.

[10] Sailer S., Leine R.I. (2021) Model reduction of the tippedisk: a path to the full analysis. *Nonlinear Dyn.* **105**:1955–1975.

[11] Sailer S., Leine R.I. (2021) Singularly perturbed dynamics of the tippedisk. *Proc. R. Soc. A.* **477**.

[12] Shchepakina E., Sobolev V., Mortell M.P. (2014) Singular Perturbations. Springer International Publishing.